Design Optimization of a Very High Power Density Motor with a Reluctance Rotor and a Modular Stator Having PMs and Toroidal Windings

Peng Han*, *Senior Member, IEEE*, Murat G. Kesgin, *Student Member, IEEE*, Dan M. Ionel, *Fellow, IEEE*, Rohan Gosalia[1], Nakul Shah[1], Charles J. Flynn[1], Chandra Sekhar Goli[2], *Student Member, IEEE*, Somasundaram Essakiappan[3], *Senior Member, IEEE*, and Madhav Manjrekar[2], *Senior Member, IEEE*

SPARK Laboratory, ECE Department, University of Kentucky, Lexington, KY, USA
[1]QM Power, Inc., Kansas City, MO, USA
[2]Dept. of Electrical and Computer Engineering, University of North Carolina at Charlotte, Charlotte, NC, USA
[3]Energy Production and Infrastructure Center, University of North Carolina at Charlotte, Charlotte, NC, USA

peng.han@ieee.org, murat.kesgin@uky.edu, dan.ionel@ieee.org, rgosalia@qmpower.com, nshah@qmpower.com, jflynn@qmpower.com, cgoli@uncc.edu, somasundaram@uncc.edu, madhav.manjrekar@uncc.edu

Abstract: This paper proposes a new high power density permanent magnet (PM) motor design for traction applications to achieve the 50kW/L target set by the US Department of Energy by increasing the torque capability and operating speed compared to conventional PM machine topologies. A large-scale multi-objective design optimization based on 2D finite element analysis (FEA) and differential evolution algorithm was conducted to achieve the best trade-off among high efficiency, high power density and high power factor. The torque-speed envelopes are also checked for the Pareto front designs to make sure they have a constant power speed ratio of at least 3:1. An open frame lab prototype (OFLP) motor has been fabricated and tested to validate the principle of operation and design optimization approach, and to identify the potential challenges in manufacturing and testing. Ongoing work on further pushing the electromagnetic performance to the limit and improving the manufacturing and cooling techniques are also discussed.

***Index Terms*—Design optimization, electric machine, high power density, modularization, multi-objective, permanent magnet, reluctance machine**

I. Introduction

The U.S. DRIVE Electrical & Electronics Technical Team Roadmap (2017) identified key challenges and R&D targets for electric traction drive systems for the year 2025, which mainly include a power density requirement of 50kW/L for the motor, 100kW/L for the accompanying power electronics, and an overall system figure of 33kW/L [1]. This represents an ambitious 89% reduction in motor volume compared to 2020 targets. Representative electric machines used in state-of-the-art commercially available electric vehicles (EVs) and hybrid EVs (HEVs), mainly the induction machines and interior permanent magnet (IPM) machines, have been surveyed in [2]. Innovative motor and drive technologies having the potential to meet the DOE 2025 targets are, therefore, in great need.

Synchronous machines with PMs in the rotor have been continuously developed for increasing specific power capability. In order to achieve very high magnetic loading, the "spoke" IPM configuration with radially oriented and tangentially magnetized PMs has been employed in conjunction with, for example: q-axis flux barriers [3], special stator tooth profiles [4], and high-polarity fractional slot-pole combinations, leading to high-performance demonstrators for special applications, such as Formula E traction motors [5]. A major challenge for PM synchronous motor designs is the cooling of the rotor in order to avoid the risks of PM overheating and demagnetization [6]. Alternative solutions are provided by machines in which both the armature windings and the PMs, possibly in a "spoke" arrangement for flux focusing, are placed in the stator. Examples of such machine concepts include: doubly salient PM (DSPM) [7], flux-reversal PM [8], flux-switching PM [9], [10], and, more recently, switched reluctance with PMs [11] motor types.

By placing PMs in the stator yoke or teeth, the risk of demagnetization by armature field can be minimized. In addition, since the rotors are simple reluctance structures, such machines are very suitable for high-speed operation and thus high power density design. This paper presents the theoretical analysis, design optimization, and experimental study of a reluctance machine with both PMs and armature windings on the stator aiming at the 50kW/L power density target. Special care was considered for the stator core modularization, PM segmentation, winding structure, and cooling system to maximize the power density.

The rest of this paper is organized as follows. Section II presents the construction of the proposed high power density PM motor. Section III analyzes the operating principle and torque production mechanism based on the air-gap flux density waveforms and the principle of virtual work. Multi-objective

*Dr. Peng Han was with the SPARK Laboratory, ECE Department, University of Kentucky, Lexington, KY and is now with Ansys Inc., San Jose, CA USA

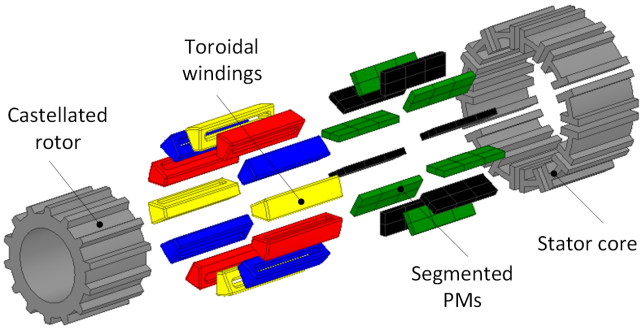

Figure 1. Exploded view of the proposed PM motor. The PM-free castellated rotor, modular stator, segmented PMs, and concentrated toroidal windings are the key features.

design optimization based on 2D FEA is presented in Section IV, followed by the prototyping and experimental testing of a low-power design in section V. Section VI discusses the plan for further power density improvement and Section VII concludes the full paper.

II. Proposed Very High Power Density PM Motor

The proposed very high power density PM motor derived from the parallel path magnetic technology [12], [13] has a PM-free castellated reluctance rotor, a modular stator having concentrated toroidal coils and circumstantially magnetized PMs, as illustrated in Fig. 1. The robust rotor construction is very suitable for high-speed operation. In addition, since both the PMs and armature windings are placed on the stator and there is no overlapping between them, the design and implementation of the cooling system are expected to be significantly simplified.

The toroidal windings are naturally concentrated, therefore, the copper slot fill is improved and the end coils are shortened compared to conventional distributed windings, which lead to reduced dc copper loss. The adjacent magnets are magnetized in the opposing way, as shown in Fig. 2, to provide the desired flux coupling for torque enhancement [12], [13]. The combination of stator PMs, rotor protrusions and stator winding layout plays a key role in determining the overall electromagnetic performance, such as average torque, torque ripple, power factor, etc, which will be shown in Section III.

III. Theoretical Analysis of Operating Principle and Torque Production

To show the operating principle and torque production mechanism of the proposed motor, both the open-circuit (OC) PM field and OC armature field are analyzed based on the simple MMF-permeance model illustrated in Fig. 3. In analyzing the OC PM field, the armature windings are removed and PMs are the only source of the magnetic field.

Neglecting the slotting effect of the stator, the air-gap flux density distribution produced by PMs can be expressed concisely as (1),

$$
\begin{aligned}
&B_{PM}(\phi,t) = \\
&\frac{F_{PM}}{2h+1}\Bigg\{\left(\frac{\Lambda_{max}+\Lambda_{min}}{2}\right)\sin\left[(2h+1)p_m(\phi-\phi_0)\right] \\
&+\left(\frac{\Lambda_{max}-\Lambda_{min}}{4}\right)\sin\left[(2h+1)p_m+N_r\right]\cdot \\
&\left[\phi-\frac{N_r\omega_r}{(2h+1)p_m+N_r}t-\frac{(2h+1)p_m\phi_0+N_r\theta_{r0}}{(2h+1)p_m+N_r}\right] \\
&+\left(\frac{\Lambda_{max}-\Lambda_{min}}{4}\right)\sin\left[(2h+1)p_m-N_r\right]\cdot \\
&\left[\phi-\frac{-N_r\omega_r}{(2h+1)p_m-N_r}t-\frac{(2h+1)p_m\phi_0-N_r\theta_{r0}}{(2h+1)p_m-N_r}\right]\Bigg\},
\end{aligned}
\tag{1}
$$

where $B_{PM}(\phi,t)$ is the air-gap flux density distribution produced by PMs only. F_{PM} is the amplitude of the square-wave MMF created by PMs. Λ is the air-gap permeance, the subscripts "max" and "min" of which denote the maximum and minimum value, respectively. p_m is the principal pole pairs of the PM array, which is half of the number of PMs. ϕ is the mechanical angle along the air-gap peripheral. ϕ_0 is the initial position from the reference axis. h is a positive integer. N_r is the number of rotor protrusions. ω_r is the mechanical rotor speed, and θ_{r0} the initial rotor position. t is time.

Equation (1) shows that there are three groups of flux density harmonics in the air gap when only the PMs are considered as the source, whose pole pairs are $(2h+1)p_m$, $(2h+1)p_m+N_r$ and $|(2h+1)p_m-N_r|$. In addition, their rotating speeds are different.

Similarly, the air-gap flux density distribution $B_{AR}(\phi,t)$ produced by the armature windings solely can also be obtained, as expressed by (2),

$$
\begin{aligned}
&B_{AR}(\phi,t) = \frac{3W_{max}I_m}{\pi}\Bigg\{\left(\frac{\Lambda_{max}+\Lambda_{min}}{2}\right)\cdot \\
&\sum_{n=3r+1=tp_a}^{\infty}\frac{1}{(n/p_a)}\sin n\left[\phi-\left(\frac{\omega}{n}\right)t-\left(\phi_{a0}-\frac{\varphi_a}{n}\right)\right] \\
&+\left(\frac{\Lambda_{max}-\Lambda_{min}}{4}\right)\sum_{n=3r+1=tp_a}^{\infty}\frac{1}{(n/p_a)}\sin\left(n+N_r\right)\cdot \\
&\left[\phi-\left(\frac{\omega-N_r\omega_r}{n+N_r}\right)t-\left(\frac{n\phi_{a0}+N_r\omega_r-\varphi_a}{n+N_r}\right)\right] \\
&+\left(\frac{\Lambda_{max}-\Lambda_{min}}{4}\right)\sum_{n=3r+1=tp_a}^{\infty}\frac{1}{(n/p_a)}\sin\left(n-N_r\right)\cdot \\
&\left[\phi-\left(\frac{\omega+N_r\omega_r}{n-N_r}\right)t-\left(\frac{n\phi_{a0}-N_r\omega_r-\varphi_a}{n-N_r}\right)\right]\Bigg\},
\end{aligned}
\tag{2}
$$

where $B_{AR}(\phi,t)$ is the air-gap flux density distribution pro-

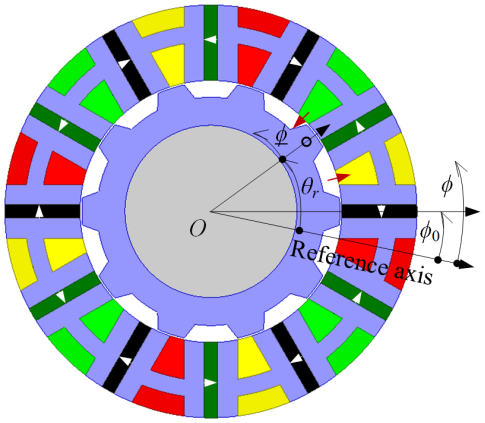

Figure 2. Cross-sectional view of the design with 10 rotor protrusions.

duced by armature windings only. W_{max} is the peak value of the sawtooth-wave winding function and I_m the peak value of phase current. p_a is the principal pole pairs of the armature winding, which is the same as the number of coils per phase. n, r, and t are positive integers. ω is the electrical frequency of winding currents, and φ_a the phase angle. ϕ_{a0} is the angle from the reference axis to the phase-A winding axis. There are also three groups of air-gap flux density harmonics, whose pole pairs are $n = 3r + 1 = tp_a$, $n + N_r$ and $|n - N_r|$.

With the closed-form analytical air-gap flux density distributions $B_{PM}(\phi, t)$ and $B_{AR}(\phi, t)$, the electromagnetic torque can be derived by using the principle of virtual work:

$$T_{em} = \frac{\partial W_{co}}{\partial \theta_r} = \frac{\partial}{\partial \theta_r} \int_V \frac{\{B_{PM}(\phi,t) + B_{AR}(\phi,t)\}^2}{2\mu_0} dV. \quad (3)$$

By applying the orthogonality relations of sine functions to (3), it can be drawn that only the flux density harmonics from the PM field and armature field of the same pole pairs will produce the non-zero average torque. As a result, the average electromagnetic torque of this motor is contributed by multiple dominating air-gap flux density harmonics, whose pole pairs of 4, 6, 8, 16, 18 and 28.

It is also revealed that there will be no torque, if one of the following is absent: stator PMs which are denoted by F_{PM} in (1), current in stator toroidal coils, or the rotor with protrusions denoted by Λ_{max} and Λ_{min}. The castellated reluctance rotor serves mainly as a modulator to couple PMs and armature windings through air-gap flux density harmonics and there is virtually no synchronous type reluctance torque, i.e., the torque component proportional to the product of d-axis and q-axis currents in conventional synchronous machines.

In addition, by examining terms in (3), the appropriate combinations of stator PMs, rotor protrusions, and stator winding layouts producing non-zero average torques can be readily identified. Typical topologies derived from this approach include the 5-protrusion (5-P) and 7-protrusion (7-P) designs for a stator with 6 PMs and 6 toroidal coils, and the 10-protrusion (10-P) and 14-protrusion (14-P) designs for a stator with 12 PMs and 12 toroidal coils.

Equations (1)-(3) well explain the operating principle and torque production mechanism of the proposed motor, but are not suitable for accurate force/torque computation. The Maxwell stress tensor method is used instead. The radial and tangential components of the electromagnetic stress in the airgap, f_r, and ,f_t, can be expressed by the following:

$$f_r(\phi,t) = \frac{B_r(\phi,t)^2 - B_t(\phi,t)^2}{\mu_o}, \quad (4)$$

$$f_t(\phi,t) = \frac{B_r(\phi,t)B_t(\phi,t)}{\mu_o}, \quad (5)$$

where $B_r(\phi, t)$ and $B_t(\phi, t)$ are the radial and tangential air-gap flux densities calculated by FEA. The radial and tangential force on the stator teeth and rotor protrusions can be obtained by integrating the corresponding stress component over circumferential intervals, as shown by the example in Fig. 4 and Fig. 5. Radial component of force density is substantially higher than tangential components. Radial force of stator tooth modules which is two stator teeth and magnet between them at given rotor position can be seen in Fig. 6. Torque contribution of each stator tooth module is different from each other, but half motor symmetry can be see in Fig. 7.

Average torque contributed by stator teeth, magnets, and coils are calculated for the studied machine from this approach. The produce majority of the torque is produced by the leading teeth located at the left-hand side of magnets when looking into the page. Torque produced by magnets and the tracking teeth located other side of the magnet almost cancel each other. Coils contribute little torque.

IV. Multi-objective Design Optimization Based on 2D FEA

Parametric models for a number of motor topologies were developed following the derived combinations from Section III. Based on the parametric electromagnetic FEA models for the 5-P, 7-P, 10-P and 14-P designs illustrated in Fig. 2 with 10 independent geometric and control variables, a large-scale design optimization was performed, following the optimization approach used in, for example, [14], [15]. The objective was to maximize the power density with a 50kW/L target, efficiency and power factor, assuming an equivalent electric loading, i.e., the product of current density and copper slot fill factor, equal to 9.75A/mm^2 can be achieved by the cooling design and advanced winding technology. The results of optimization studies indicated that specific torque increases with number of rotor protrusions, and so do core losses, in line with expectations.

A systematic comparative study between two motor topologies was also carried out based on multi-objective design optimizations, one with 10-P and the other 14-P, as shown in Fig. 8. The three concurrent objectives were to maximize the power density, minimize the total loss, and maximize the power factor. The computational results show that, the optimal 14-P designs can achieve similar fundamental power factors as optimal 10-P designs. There are trade-offs between 10-P and 14-P designs in terms of the power density and total loss (Fig. 9).

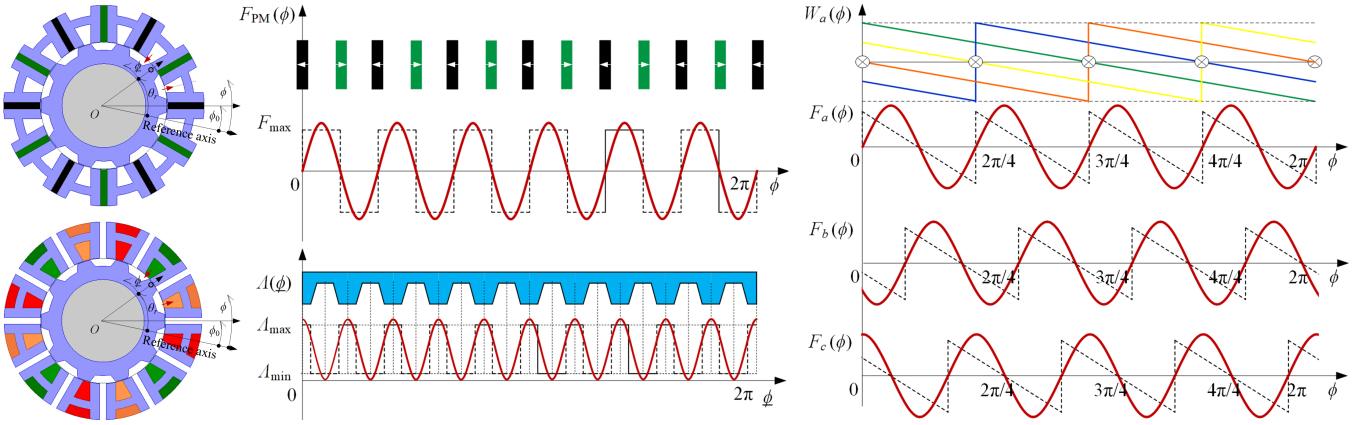

Figure 3. Simple MMF-permeance models for the proposed motor with PMs only and armature windings only. The fundamental components of the air-gap permeance function and winding functions of armature coils are used for derivation. The winding functions of the toroidal windings are sawtooth waves, which are very different from the conventional slot windings.

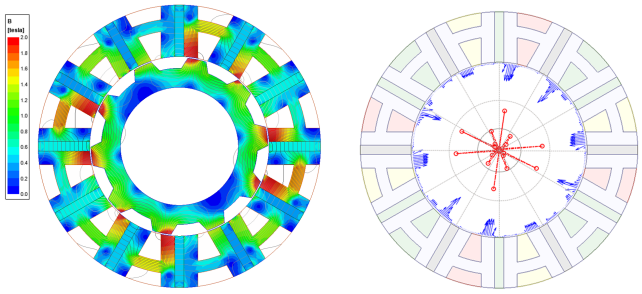

Figure 4. FEA results of the proposed motor at rated load, (a) flux density distribution and flux pattern, (b) electromagnetic force on stator teeth. Blue arrows denote the distributed force vectors and red dots denote the resultant forces on teeth.

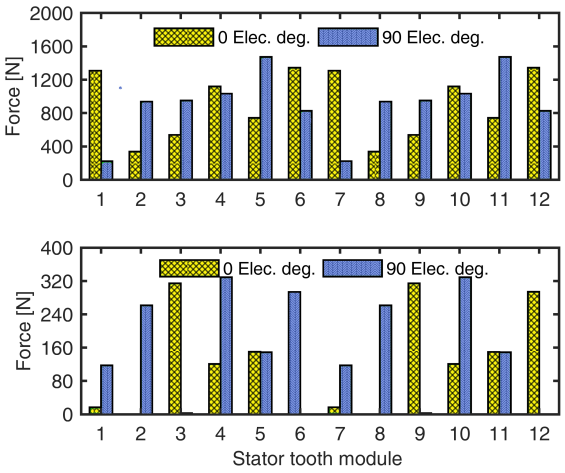

Figure 6. Radial (top) and tangential (bottom) force on the stator tooth module at different rotor position under rated-load.

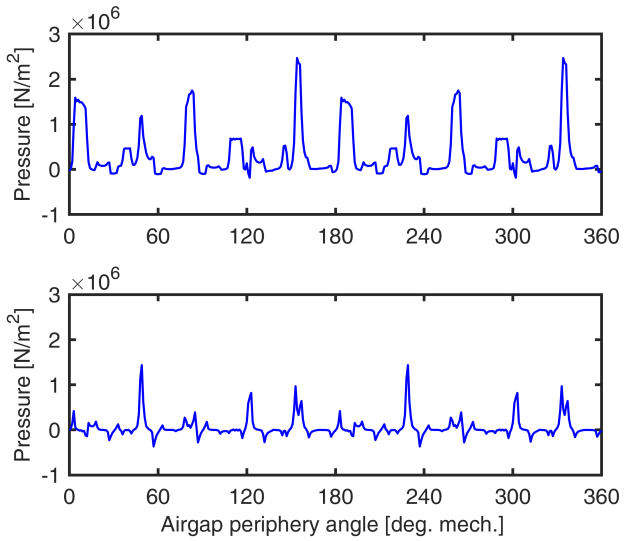

Figure 5. Air-gap stresses at rated load: radial component (top), (b) tangential component (bottom).

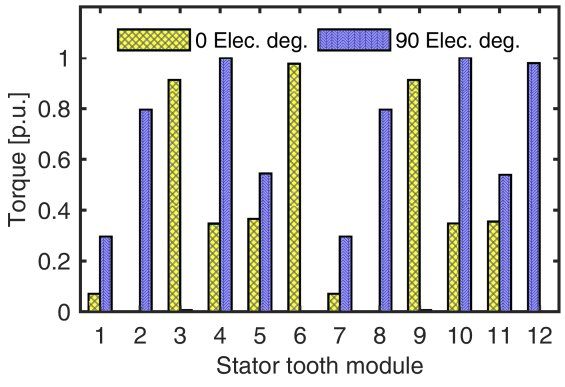

Figure 7. Electromagnetic torque contribution of each stator module at different rotor position under rated-load.

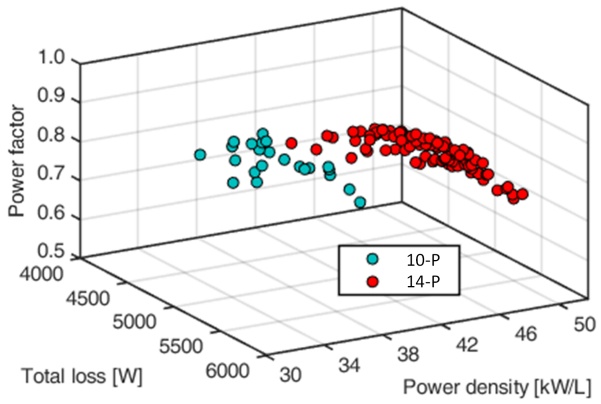

Figure 8. Optimization results: 3D Pareto front projection with objectives of total loss, power density, and power factor.

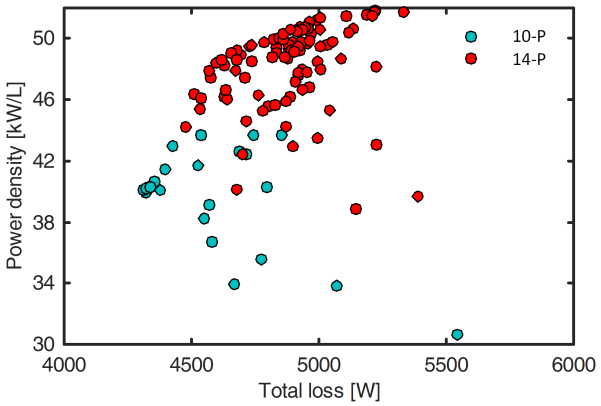

Figure 9. Optimization results projection in total loss - power density plane.

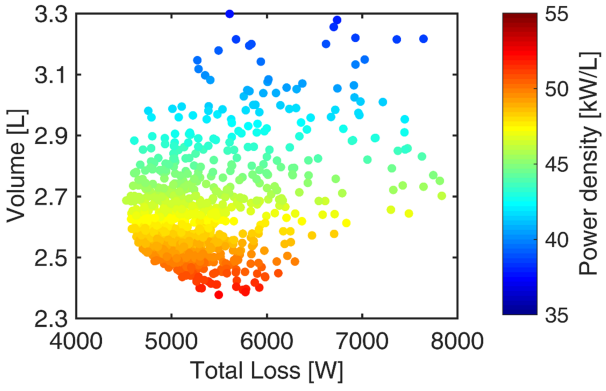

Figure 10. Optimization results: Pareto front of total loss and volume.

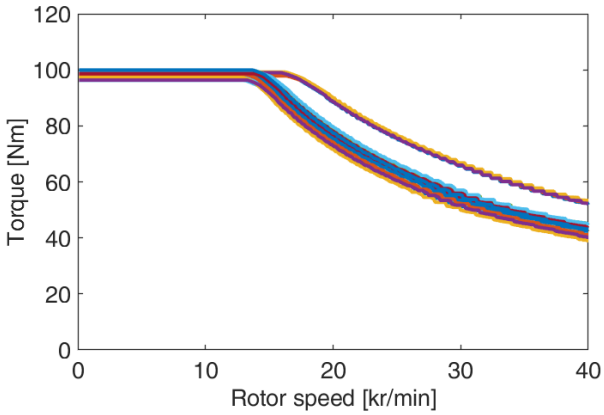

Figure 11. Torque-speed envelops of the Pareto front designs.

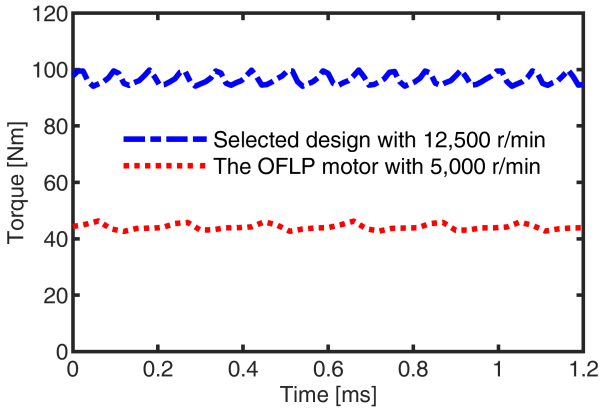

Figure 12. Torque waveform for high power density optimal design and its OFLP version. Low torque ripple is observed for both operation points.

Multiple design generations of the adopted differential evolution optimization yielded a satisfactory Pareto front. A number of candidate designs were identified, with estimated power density ≥ 50kW/L, as shown in Fig. 10. The torque-speed and efficiency maps have also been calculated based on 2D electromagnetic FEA, as plotted in Fig. 11, showing that the optimally designed motor can operate with a constant power of 125kW at up to 3 times the base speed, which is 12,500r/min. The selected optimal design for the proposed topology produces 96Nm at 12,500r/min. The waveform of the OFLP motor and the optimal design can be seen Fig. 12.

V. Experimental Testing of Open Frame Lab Prototype Motor

To validate the proposed very high power density motor and the adopted design optimization approaches, as well as to identify the potential challenges in manufacturing and testing to achieve the final goal of 50kW/L, a 28hp OFLP motor rated at 40Nm and 5,000r/min was fabricated, as shown in Fig. 13, and tested.

The experimental testing was conducted to measure the OC back-electromotive force (EMF) for a single phase with 4 coils connected in series, as plotted in Fig. 14, showing good

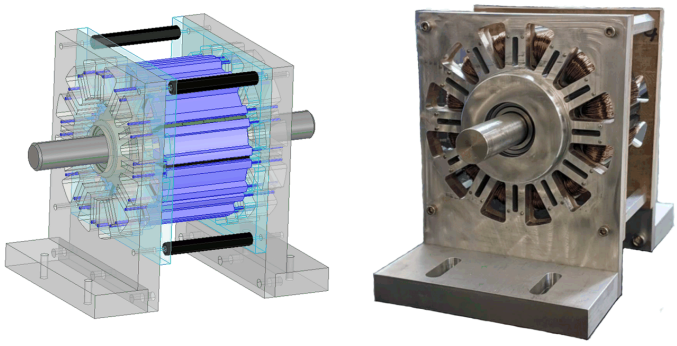

Figure 13. The CAD drawing and photo of the full assembly for the open frame lab prototype motor. Dowel pins were used in the laminated stator segments. PMs were segmented in both radial and axial directions to reduce the PM eddy current losses. All the coil terminals have been brought out for detailed testing purpose.

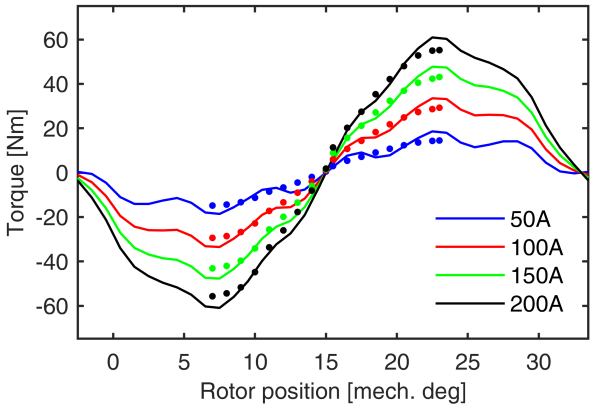

Figure 15. Testing results of torque measured static torque versus rotor positions (continuous lines – FEA results, dots – experimental measurements)

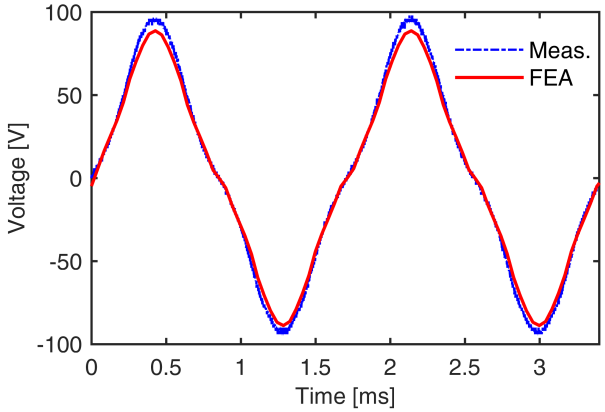

Figure 14. Simulated and experimental open-circuit back EMF for phase-A winding.

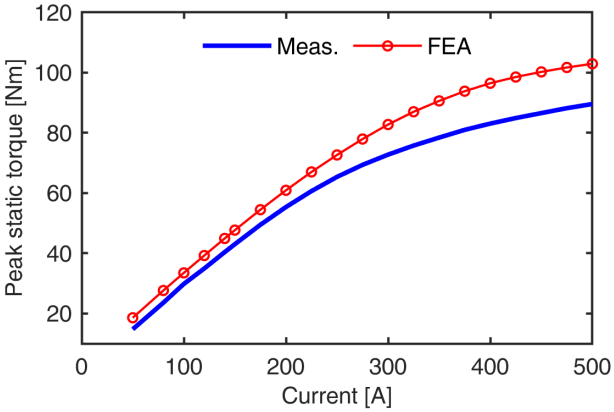

Figure 16. Testing and simulation results of peak torque versus different current values.

agreement between the experimental measurements and 2D FEA calculations.

The static torques at different rotor positions were also measured when the phase-A winding was connected in series with the parallel of phase-B and phase-C windings. Each phase has 4 coils connected in series. It is shown that, within the expectation, the measured static torque has the same trend as the 2D FEA as seen in Figs 15 and 16. The deviation is approx. 10% and can be explained by the backlash of the locking device, especially at the high torque region, the temperature rise, the inaccuracies of material properties, etc.

VI. Discussions

The OFLP motor achieves a power density of 8.4kW/L at 5,000r/min with an open housing for air cooling. The reduced power density is attributed to the low copper slot fill of 0.41 achieved by hand wound wired coils, the reduced speed due to the limitations of current testing facilities, and the reduced current density to prevent overheating with the air cooling. The 50kW/L target is anticipated to be achieved by improving the copper slot fill to 0.75-0.8 by advanced winding technologies, for example, the additively manufactured coils [16], and increasing the current density to produce higher torque enabled by the advanced cooling technologies, such as the one presented in [17], and operate the motor at the designed rated speed of 12,500r/min.

In the meantime, reducing the losses, mainly the core losses, by reducing the number of rotor protrusions and therefore the fundamental driving frequency is underway to simplify the cooling design. Reducing the fundamental frequency will also benefit the control system and reduce the switching frequency.

VII. Conclusion

Through the systematic design optimization study and prototyping exercise presented in this paper. The proposed motor has numerous advantages for high power density designs, such as the high-speed operation capability, better cooling design, compact winding structure, modularized manufacturing of the stator, and an inherent wide speed range with a constant power speed ratio of at least 3:1. Appropriate combinations of stator PMs, stator windings, and rotor protrusions are required to produce high torque. The electromagnetic performance trade-offs mainly lie between the power density and efficiency, and large-scale design optimizations are required to achieve the

optimal designs in the sense of multiple objectives. Advanced winding technologies that can substantially increase the copper slot fill and cooling techniques that can effectively dissipate the heat generated by losses in the stator are two enabling technologies to achieve the 50kW/L target for the proposed topology.

VIII. Acknowledgment

This work was supported by the Vehicle Technologies Office, U.S. Department of Energy, under award no. DEEE0008871. The material presented in this paper do not necessarily reflect the views of the U.S. Department of Energy. The authors would also like to gratefully acknowledge the direct support provided by QM Power, Inc and Ansys, Inc.

References

[1] "U.S. drive electrical and electronics technical team roadmap," Oct. 2017. [Online]. Available: https://www.energy.gov/eere/vehicles/downloads/us-drive-electrical-and-electronics-technical-team-roadmap

[2] I. Husain, B. Ozpineci, M. S. Islam, E. Gurpinar, G. J. Su, W. Yu, S. Chowdhury, L. Xue, D. Rahman, and R. Sahu, "Electric drive technology trends, challenges, and opportunities for future electric vehicles," *Proc. IEEE*, pp. 1–21, 2021.

[3] D. Ionel, J. Eastham, and T. Betzer, "Finite element analysis of a novel brushless dc motor with flux barriers," *IEEE Transactions on Magnetics*, vol. 31, no. 6, pp. 3749–3751, 1995.

[4] M. G. Kesgin, P. Han, D. Lawhorn, and D. M. Ionel, "Analysis of torque production in axial-flux vernier pm machines of the MAGNUS type," in *2021 IEEE International Electric Machines Drives Conference (IEMDC)*, 2021, pp. 1–5.

[5] A. Fatemi, D. M. Ionel, M. Popescu, Y. C. Chong, and N. A. O. Demerdash, "Design optimization of a high torque density spoke-type pm motor for a formula e race drive cycle," *IEEE Transactions on Industry Applications*, vol. 54, no. 5, pp. 4343–4354, 2018.

[6] S. Choi, M. S. Haque, M. T. B. Tarek, V. Mulpuri, Y. Duan, S. Das, V. Garg, D. M. Ionel, M. A. Masrur, B. Mirafzal, and H. A. Toliyat, "Fault diagnosis techniques for permanent magnet ac machine and drives—a review of current state of the art," *IEEE Trans. Transport. Electrif.*, vol. 4, no. 2, pp. 444–463, 2018.

[7] Y. Liao, F. Liang, and T. Lipo, "A novel permanent magnet motor with doubly salient structure," *IEEE Trans. Ind. Appl.*, vol. 31, no. 5, pp. 1069–1078, 1995.

[8] R. Deodhar, S. Andersson, I. Boldea, and T. Miller, "The flux-reversal machine: a new brushless doubly-salient permanent-magnet machine," *IEEE Trans. Ind. Appl.*, vol. 33, no. 4, pp. 925–934, 1997.

[9] A. S. Thomas, Z. Q. Zhu, R. L. Owen, G. W. Jewell, and D. Howe, "Multiphase flux-switching permanent-magnet brushless machine for aerospace application," *IEEE Trans. Ind. Appl.*, vol. 45, no. 6, pp. 1971–1981, 2009.

[10] T. Raminosoa, A. M. El-Refaie, D. Pan, K.-K. Huh, J. P. Alexander, K. Grace, S. Grubic, S. Galioto, P. B. Reddy, and X. Shen, "Reduced rare-earth flux-switching machines for traction applications," *IEEE Trans. Ind. Appl.*, vol. 51, no. 4, pp. 2959–2971, 2015.

[11] S. Ullah, S. McDonald, R. Martin, and G. Atkinson, "A permanent magnet assisted switched reluctance machine for more electric aircraft," in *Proc. Int. Conf. Electr. Mach. (ICEM)*, 2016, pp. 79–85.

[12] C. J. Flynn, "Parallel magnetic circuit motor," U.S. Patent 20110089775 A1, Apr. 2011.

[13] ——, "Hybrid permanent magnet motor," U.S. Patent 7898135 B2, Mar. 2011.

[14] M. Rosu, P. Zhou, D. Lin, D. M. Ionel, M. Popescu, F. Blaabjerg, V. Rallabandi, and D. Staton, *Multiphysics Simulation by Design for Electrical Machines, Power Electronics and Drives*. Wiley-IEEE Press, 201.

[15] V. Rallabandi, P. Han, J. Wu, A. M. Cramer, D. M. Ionel, and P. Zhou, "Design optimization and comparison of direct-drive outer-rotor SRMs based on fast current profile estimation and transient FEA," *IEEE Trans. Ind. Appl.*, vol. 57, no. 1, pp. 236–245, 2021.

[16] N. Simpson, C. Tighe, and P. Mellor, "Design of high performance shaped profile windings for additive manufacture," in *IEEE Energy Convers. Congr. Expo. (ECCE)*, 2019, pp. 761–768.

[17] S. A. Semidey and J. R. Mayor, "Experimentation of an electric machine technology demonstrator incorporating direct winding heat exchangers," *IEEE Trans. Ind. Electron.*, vol. 61, no. 10, pp. 5771–5778, 2014.